

1 **Intensive photochemical oxidation in the marine atmosphere:**
2 **Evidence from direct radical measurements**

3 Guoxian Zhang^{1,2}, Renzhi Hu^{1, *}, Pinhua Xie^{1,2,3, **}, Changjin Hu¹, Xiaoyan Liu⁴,
4 Liujun Zhong¹, Haotian Cai¹, Bo Zhu⁵, Shiyong Xia⁵, Xiaofeng Huang⁵, Xin Li⁶,
5 Wenqing Liu¹

6 ¹ Key Laboratory of Environment Optics and Technology, Anhui Institute of Optics and Fine
7 Mechanics, HFIPS, Chinese Academy of Sciences, Hefei, China

8 ² University of Science and Technology of China, Hefei, China

9 ³ College of Resources and Environment, University of Chinese Academy of Science, Beijing,
10 China

11 ⁴ School of Pharmacy, Anhui Medical University, Hefei, China

12 ⁵ Key Laboratory for Urban Habitat Environmental Science and Technology, School of
13 Environment and Energy, Peking University Shenzhen Graduate School, Shenzhen, China

14 ⁶ State Key Joint Laboratory of Environmental Simulation and Pollution Control, College of
15 Environmental Sciences and Engineering, Peking University, Beijing, China

16

17 ***Correspondence to:** Renzhi Hu, Key Laboratory of Environment Optics and
18 Technology, Anhui Institute of Optics and Fine Mechanics, HFIPS, Chinese Academy
19 of Sciences, Hefei, China

20 ****Correspondence to:** Pinhua Xie, University of Science and Technology of China,
21 Hefei, China

22 **Email addresses:** rzhu@aiofm.ac.cn (Renzhi Hu); phxie@aiofm.ac.cn (Pinhua Xie)

23

24 **Abstract:** Comprehensive observations of hydroxyl (OH) and hydroperoxy (HO₂)
25 radicals were conducted in October 2019 at a coastal continental site in the Pearl
26 River Delta (YMK site, 22.55°N, 114.60°E). The daily maximum OH and HO₂
27 concentrations were $(4.7\text{--}9.5) \times 10^6 \text{ cm}^{-3}$ and $(4.2\text{--}8.1) \times 10^8 \text{ cm}^{-3}$, respectively. The
28 synchronized air mass transport from the northern cities and the South China Sea
29 exerted a time-varying influence on atmospheric oxidation. Under a typical ocean-
30 atmosphere (OCM), reasonable measurement model agreement was achieved for both
31 OH and HO₂ using a 0-D chemical box model incorporating the regional atmospheric
32 chemistry mechanism version 2-Leuven isoprene mechanism (RACM2-LIM1), with
33 daily averages of $4.5 \times 10^6 \text{ cm}^{-3}$ and $4.9 \times 10^8 \text{ cm}^{-3}$, respectively. Land mass (LAM)
34 influence promoted more active photochemical processes, with daily averages of 7.1
35 $\times 10^6 \text{ cm}^{-3}$ and $5.2 \times 10^8 \text{ cm}^{-3}$ for OH and HO₂, respectively. Heterogeneous uptake
36 had certain effects on HO_x chemistry, but the influence of the halogen mechanism
37 was limited by NO_x level. Intensive photochemistry occurred after precursor
38 accumulation, allowing local net ozone production comparable with surrounding
39 suburban environments (5.52 ppb/h during the LAM period). Rapid oxidation process
40 was accompanied by a higher diurnal nitrous acid (HONO) concentration (> 400 ppt).
41 After a sensitivity test, HONO-related chemistry elevated the ozone production rate
42 by 33% and 39% during the LAM and OCM periods, respectively. The nitric acid
43 (P(HNO₃)) and sulfuric acid (P(H₂SO₄)) formation rates also increased
44 simultaneously (~43% and ~48% for LAM and OCM sectors, respectively). In the
45 ozone-prediction test, simulated O₃ decreased from ~75 ppb to a global background
46 (~35 ppb) without the HONO constraint, and daytime HONO concentrations were
47 reduced to a low level (~70 ppt). For coastal cities, the particularity of the HONO
48 chemistry tends to influence the ozone-sensitive system and eventually magnifies the
49 background ozone. Therefore, the promotion of oxidation by elevated precursors
50 deserves a lot of attention when aiding pollution mitigation policies.

51 **Keywords:** FAGE-LIF; OH and HO₂ radicals; Atmospheric oxidation; Marine
52 boundary layer; Precursors;

53 1 Introduction

54 The marine boundary layer (MBL) occupies 71% of the planetary boundary layer,
55 is a massive active carbon sink on Earth, and plays an irreplaceable role in coping
56 with global climate change (Stone et al., 2012; Woodward-Massey et al., 2022b; Liu
57 et al., 2022a). As a typical background atmosphere on the Earth, the MBL is
58 equivalent to a natural smog chamber with limited anthropogenic emissions and is
59 characterized by low NO_x (the sum of nitric oxide (NO) and nitrogen dioxide (NO₂))
60 and non-methane hydrocarbons (NMHCs) under a layer of clean air (Woodward-
61 Massey et al., 2022b). The lifetime of OH radical, a key oxidant, is on the order of a
62 few hundred milliseconds (Fuchs et al., 2012). Due to the scarcity of oxidation
63 precursors, including nitrous acid (HONO), formaldehyde (HCHO), and NMHCs, the
64 reaction between O¹D and water vapor generally dominates the radical initiation
65 pathway in the marine environment. For example, in a tropical boundary layer
66 observation experiment (reactive halogens in the marine boundary layer, RHaMBLe),
67 ozone photolysis was found to account for 70% of the OH radical source based on the
68 master chemical mechanism (MCM) (Whalley et al., 2010). The vital role of ozone
69 photolysis is contrasting with typical polluted and semi-polluted areas investigated in
70 a series of field campaigns, in which the propagation routes were found to dominate
71 the radical source (Yang et al., 2021a; Tan et al., 2019a). Therefore, studying the
72 radical chemistry in the MBL provides a valuable opportunity to test the current
73 understanding of atmospheric oxidation mechanisms in a natural setting.

74 Since the earliest observations off the coast of northern Norfolk in the Weybourne
75 Atmospheric Observatory Summer Experiment in June 1995 (WAOSE95), more
76 observations and simulations of radical chemistry in the MBL environment have been
77 conducted using ground-based, airborne, and shipborne instruments (Qi et al., 2007;
78 Kanaya et al., 2002; Kanaya et al., 2001; Mallik et al., 2018; Woodward-Massey et al.,
79 2022a; Carpenter et al., 2011; Grenfell et al., 1999; Brauers et al., 2001; Whalley et al.,
80 2010). Most field measurements have yielded well-reproduced OH and HO₂
81 concentration profiles via chemical mechanisms, with differences of within ~20%.

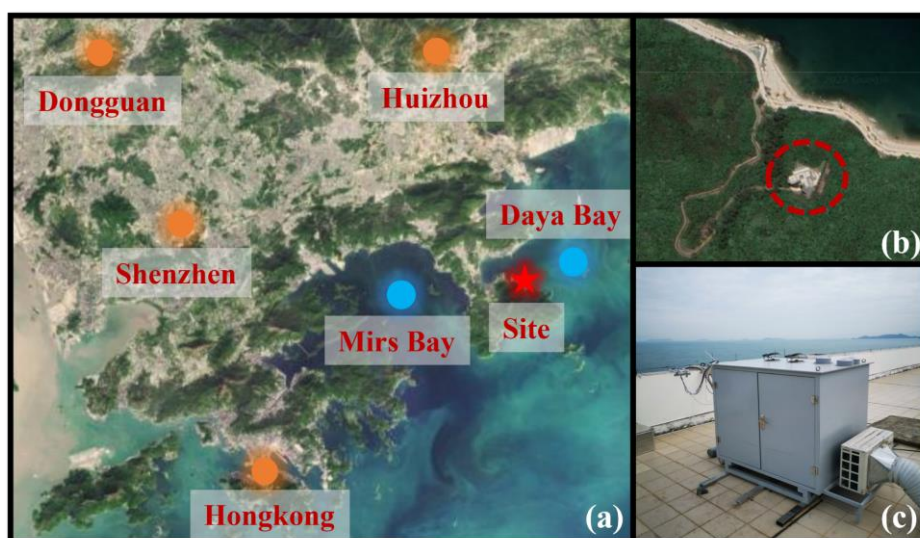
82 However, the base model is not sufficient to describe the radical chemistry in some
83 exceptional cases, especially in regard to the HO₂ radical. Considering the practical
84 association between halogen (Cl, Br, and I) chemistry and heterogeneous chemistry in
85 marine new particle formation, particularly the involvement of heterogeneous iodine-
86 organic chemistry, exploring the synchronous influence of these mechanisms on HO_x
87 (OH and HO₂) radical chemistry in the MBL region is a worthy endeavor (Xu et al.,
88 2022; Huang et al., 2022). The mixing of air masses of continental and marine origins
89 can lead to more variability in radical concentrations. During seasonal measurements
90 of both OH and HO₂ in the Atlantic Ocean, variance analysis indicated that around 70%
91 of the variance of OH and HO₂ was due to diurnal behavior (in the form of photolysis
92 frequency), while the remaining variance was attributed to long-term seasonal cycles
93 (in the form of the changes in O₃, CO and air mass contribution) (Vaughan et al.,
94 2012).

95 The Chinese economy has undergone rapid development in recent years, and the
96 co-occurrence of primary and secondary regional pollution has become a severe
97 problem (Lu et al., 2019; Liu et al., 2022c). The interactions between air pollutants
98 from upwind cities, shipping vessels, and other anthropogenic emissions lead to
99 precursor accumulation (Sun et al., 2020; Zeren et al., 2022). The background ozone
100 concentration in key regions of China has increased year by year, highlighting the
101 significant influence of anthropogenic activities on the atmospheric oxidation in
102 background regions in China (Wang et al., 2009; Chen et al., 2022). However, little
103 research has been dedicated to the radical chemistry and oxidation mechanism in
104 regions with both coastal and continental features. To fill this research gap, in this
105 study, a field campaign was conducted on photochemistry in the MBL at a coastal site
106 in the Pearl River Delta. The OH and HO₂ radicals associated with other related
107 species were measured in October 2019, and the radical-related oxidation process was
108 identified to determine the photochemical efficiency in the marine atmosphere.

109 **2 Materials and methods**

110 2.1 Site description

111 As shown in Fig. 1(a), this observation campaign lasted for 11 days from
112 October 18 to October 28, 2019, in Yangmeikeng (YMK, 22.55°N, 114.60°E), a
113 coastal site in Shenzhen, Pearl River Delta. As the core city of the Greater Bay Area,
114 Shenzhen is bordered by Dongguan to the north, Huizhou to the east, and Hong Kong
115 to the south. The YMK site is on the Dapeng Peninsula, to the southeast of Shenzhen,
116 between Mirs Bay and Daya Bay. As it is adjacent to the port of Hong Kong,
117 precursors from ship emissions may influence the atmospheric chemistry. The site is a
118 part of Shenzhen Ecological Monitoring Center station, approximately 35 m above
119 sea level, and the sea is approximately 150 m to the east. No apparent local emissions
120 exist, and the surrounding forest is lush (Fig. 1(b)). Previous literatures reported the
121 monoterpene concentration in the YMK site, with a daily mean of 0.187 ppb (Zhu et
122 al., 2021). Abundant biogenic emissions will likely influence the local chemistry. In
123 addition to anthropogenic and vegetation emissions, the site is also affected by the
124 synchronization of plumes from northern cities and the South China Sea (Niu et al.,
125 2022; Xia et al., 2021). Due to its significant time-varying pollution characteristics,
126 this area is an ideal site for studying the effects of plume transport on atmospheric
127 oxidation.



128

129 **Fig. 1.** Details of the observation site.(a) The location of the measurement site and surrounding cities. The satellite
130 map data is extracted from Google Earth.(b) Th close shot of the measurement site location.(c) The actual image
131 for the LIF-Box.

132 Using the hybrid single-particle Lagrangian integrated trajectory (HYSPLIT)

133 model, the 24-h backward trajectories on special days were obtained. In Fig. S1, the
134 red, blue, and green trajectories represent the results at altitudes of 100, 500, and 1000
135 m above ground level, respectively. Two typical transportation pathways dominated
136 the air parcels. One originated from the northern megacities in the Pearl River Delta
137 (defined as the land mass, LAM), especially on October 18, 19, and 27. In contrast, a
138 clean air mass from the east or northeast was mainly transported to the observation
139 site from the ocean (defined as the ocean mass, OCM), with representative episodes
140 on October 22, 25, and 26.

141 **2.2 Instrumentation**

142 **2.2.1 HOx radical measurements**

143 The OH and HO₂ radicals were measured via laser-induced fluorescence (LIF).
144 The OH radical can be directly measured by exciting the fluorescence using a 308-nm
145 laser. HO₂ is converted into the OH radical via chemical transformation and then
146 detected in the form of OH radical. The self-developed instrument, the Anhui Institute
147 of Optics Fine Mechanics-LIF (AIOFM-LIF), was used to conduct the measurements
148 (Zhang et al., 2022a; Wang et al., 2021; Wang et al., 2019). This system has been used
149 in key regions of China, including the Yangtze River Delta, Pearl River Delta, and
150 Chengdu-Chongqing region, and achieved good performance in a comparison
151 experiment with a LIF system jointly developed by Forschungszentrum Jülich and
152 Peking University (PKU-LIF) (Zhang et al., 2022b).

153 The system and detection interference process have been described in detail in
154 previous studies (Zhang et al., 2022a). Briefly, the system consists of a laser output
155 module, a radical detection module, and a control and data acquisition module. These
156 modules are integrated into a sampling box with constant temperature and humidity
157 control (Fig. 1(c)). The laser output module is a union of an Nd:yttrium-aluminum-
158 garnet (YAG) solid-state laser, a 532-nm laser output, and a tunable dye laser. The
159 radical detection module utilized a single pass laser configuration, and the laser beam
160 had a diameter of 8 mm. OH and HO₂ fluorescence cells are combined in parallel and
161 share a common axial optical path. The 308-nm laser is introduced into the HO₂ cell

162 first and then into the OH cell via an 8-m fiber. To maintain the detection efficiency,
163 the power in the OH fluorescence cell should be at least 15 mW. In the detection
164 process, a set of lenses was deployed and positioned in front of the microchannel plate
165 detector (MCP) to boost the fluorescence collection capacity. Each MCP detector
166 contains a timing control instrument to optimize the signal-to-noise ratio (SNR) of the
167 fluorescence detection. Efficient ambient air sampling was achieved using an
168 aluminum nozzle (0.4 mm orifice), and the pressure in the chamber was maintained at
169 400 Pa via a vortex vacuum pump (XDS35i, Edwards) to reduce fluorescence
170 quenching.

171 A wavelength modulation for the background measurement that periodically
172 switches from an on-resonant state to a non-resonant state has been widely used to
173 obtain spectral zero. Since the ozone photolysis interference is due to the laser light
174 itself, wavelength modulation does not allow removing it. Through laboratory
175 experiments, at 20 mW laser energy, every 1% water vapor concentration and 50 ppb
176 ozone concentration can generate a $2.5 \times 10^5 \text{ cm}^{-3}$ OH concentration. The results in
177 this paper have subtracted the ozone photolysis interference (Fig. S2). In terms of
178 system design, the AIOFM-LIF system incorporates a short-length inlet design to
179 minimize interferences from ozonolysis and other unknown factors (the distance from
180 radical sampling to fluorescence excitation is ~ 150 mm). An OH measurement
181 comparison with an interference-free instrument, PKU-LIF, was conducted in a real
182 atmosphere in a previous study (Zhang et al., 2022b). The ozonolysis interference on
183 the measurement consistency of both systems was excluded under high-VOCs
184 condition. Overall, the key parameters related to ozonolysis reactions (O_3 , alkenes,
185 isoprene and NO_x) in YMK was similar to that during the intercomparison
186 experiment, implies that the chemical conditions do not favor the generation of
187 potential interference to OH measurement (Table S1). For HO_2 measurement, the NO
188 gas (2% in N_2) was utilized to achieve HO_2 -to-OH conversion. NO was passed
189 through a ferrous sulfate filter to remove impurities (NO_2 , HONO, and so on) before
190 being injected into the detection cell. The NO concentration ($\sim 1.6 \times 10^{12} \text{ cm}^{-3}$)

191 corresponding to a conversion efficiency of ~15% was selected to avoid RO₂→HO₂
192 interference (especially from RO₂ radicals derived from long-chain alkanes (C ≥ 3),
193 alkenes, and aromatic hydrocarbons). Previous study denoted that the percentage
194 interference from alkene-derived RO₂ under these operating conditions was no more
195 than 5% (Wang et al., 2021).

196 A standard HO_x radical source was used to complete the calibration of the
197 detection sensitivity (Wang et al., 2020). The radical source is based on the
198 simultaneous photolysis of H₂O/O₂ by a 185 nm mercury lamp. Humidified air flow is
199 introduced to produce equal amounts of OH and HO₂ radicals after passing the
200 photolysis region. The flow remained in a laminar condition with a maximum flow
201 rate of 20 SLM (standard liters per minute). As the luminous flux in photolysis region
202 is difficult to accurately measure, the linearly correlation between ozone concentration
203 and 185 nm light flux was established. Ozone concentration in the flow tube was
204 measured by a home-made Cavity Ring Down Spectrometer (CRDS, and the
205 detection limit is 15 ppt@30 s, 1σ). Mercury lamp intensity is fine-tuned to establish a
206 correlation between light intensity and ozone concentration. The instrument was
207 calibrated every 1 or 2 days (except for shutdown during rainy periods), and the
208 sensitivity used for the data processing was an average of all of the calibration results.
209 In the YMK campaign, the relative humidity varied between 40 – 80% (Fig. S3). In
210 order to test different atmospheric conditions, both low (~40%) and high (~70%)
211 levels of water vapor were selected to produce OH and HO₂ radicals for calibration,
212 and the corresponding HO_x concentration obtained from the standard source was 1.0
213 × 10⁹ cm⁻³ and 1.8 × 10⁹ cm⁻³, respectively (Zhang et al., 2022b).

214 Considering the system uncertainty and calibration uncertainty, the detection
215 limits of the OH and HO₂ radicals were 3.3 × 10⁵ cm⁻³ and 1.1 × 10⁶ cm⁻³ (60 s, 1σ),
216 respectively. At a typical laser power of 15 mW, the measurement accuracy for OH
217 and HO₂ measurement was 13% and 17% (1σ), respectively.

218 **2.2.2 Supporting measurements**

219 In addition to measuring the HO_x radicals, an extensive suite of relevant species

220 was also measured close to the LIF instrument to improve the analysis of the radical
221 photochemistry. Detailed information about the measurement instrument is presented
222 in Table S2, including the meteorological parameters (wind speed (WS), wind
223 direction (WD), temperature (T), relative humidity (RH), pressure (P), and solar
224 radiation (J-values)) and chemical parameters (ozone (O₃), carbon monoxide (CO),
225 sulfur dioxide (SO₂), HONO, NO, NO₂, HCHO, NMHCs, and particulate matter
226 (PM_{2.5})). HONO measurement was conducted using a commercial Long-Path
227 Absorption Photometer (LOPAP). The LOPAP method utilizes two absorption tubes
228 in series for differential correction, which effectively eliminates the influence of
229 known interfering substances such as NO₂ and N₂O₅, offering an advantage over
230 traditional wet chemistry methods. Zero air measurements were taken every 8 hours
231 for a duration of 20 minutes to correct for instrument baseline fluctuations. This
232 method has been extensively tested for its suitability in detecting HONO in complex
233 atmospheric conditions, as demonstrated in previous studies by (Yang et al., 2022a;
234 Yang et al., 2021b; Wang et al., 2023). Eight measured photolysis rates (j(NO₂),
235 j(H₂O₂), j(HCHO), j(HONO), j(NO₂), j(NO₃), j(O₁D)) were used as model constraints.
236 In addition to HCHO, other volatile organic compounds (VOCs) were detected using
237 a gas chromatograph coupled with a flame ionization detector and mass spectrometer
238 (GC-FID-MS). Ninety-nine types of VOCs, including C₂–C₁₁ alkanes, C₂–C₆ alkenes,
239 C₆–C₁₀ aromatics, halohydrocarbons, and some oxygenated VOCs (OVOCs), were
240 observed using the GC-FID-MS at a 1-h time interval. Only isoprene was considered
241 as a representative of biogenic VOCs (BVOCs). All of the instruments were located
242 close to the roof of the monitoring building, nearly 12 m above the ground to ensure
243 that all of the pollutants were located in a homogeneous air mass.

244 **2.3 Model description**

245 A 0-D chemical box model incorporating a condensed mechanism, the regional
246 atmospheric chemistry mechanism version 2-Leuven isoprene mechanism (RACM2-
247 LIM1), was used to simulate the radical concentrations and the generation of ozone
248 (Stockwell et al., 1997; Griffith et al., 2013; Tan et al., 2017). The meteorological

249 parameters, pollutants, and precursor concentrations mentioned in Section 2.2.2 were
 250 input into the model as boundary conditions. All of the constraints were unified to a
 251 temporal resolution of 15 min through averaging or linear interpolation. The overall
 252 average during the observations was substituted for large areas of missing data due to
 253 instrument maintenance or failure. Three days of data were entered in advance as the
 254 spin-up period, and a synchronized time-dependent dataset was eventually generated.
 255 The hydrogen (H₂) and methane (CH₄) concentrations were set to fixed values of 550
 256 ppb and 1900 ppb, respectively. The physical losses of species due to processes such
 257 as deposition, convection, and advection were approximately replaced by an 18 h
 258 atmospheric lifetime, corresponding to first order loss rate of ~1.5 cm/s (by assuming
 259 a boundary layer height of about 1 km). The sensitivity analysis shows that when the
 260 lifetime changes within 8 – 24 hours, the values differed less than 5% for both OH,
 261 HO₂, *k*_{OH} (Fig. S4). According to the measurement accuracy, the simulation accuracy
 262 of the model for the OH and HO₂ radicals was 50% (Zhang et al., 2022a).

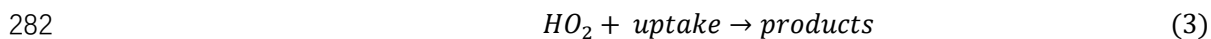
263 In addition, another steady-state calculation method (PSS) can also be used to
 264 estimate the concentrations of OH and HO₂ radicals (Eq. (1)(2), (Woodward-Massey
 265 et al., 2022b; Slater et al., 2020)). Since the *k*_{OH} and RO₂ concentrations were not
 266 obtained in this observation, simulated values are used as substitutes. Other radical
 267 and reactive intermediates are actual values that measured from the instruments in
 268 Table S2.

$$269 \quad [OH]_{PSS} = \frac{j_{HONO}[HONO] + \varphi_{OH}j(O^1D)[O_3] + k_{HO_2+NO}[NO][HO_2]}{k_{OH}} \quad (1)$$

$$270 \quad [HO_2]_{PSS} = \frac{k_{CO+OH}[CO][OH] + j_{HCHO}[HCHO] + k_{RO_2+NO}[NO][RO_2]}{k_{HO_2+NO}[NO]} \quad (2)$$

271 Considering the environmental characteristics of the MBL, the gas-phase
 272 mechanisms for bromine (Br) and iodine (I) were introduced into the base model to
 273 diagnose the impacts of the reactive bromine and iodine chemistry. The details of the
 274 mechanisms involved are listed in Tables S3 and S4. The halogen species were not
 275 available in the YMK site, so the typical levels of BrO and IO concentration in MBL
 276 site was used as a reference value (average daytime concentration of ~5 ppt) (Xia et
 277 al., 2022; Bloss et al., 2010; Whalley et al., 2010).

278 The heterogeneous uptake of HO₂ is considered to play an important role in the
279 MBL region (Whalley et al., 2010; Zou et al., 2022; Woodward-Massey et al., 2022b).
280 In order to assess the impact of HO₂ uptake on HO_x radical chemistry, we
281 incorporated HO₂ uptake reaction into the base model (Eq. (3) - (5)).



$$283 \quad k_{HO_2+uptake} = \frac{\gamma \times ASA \times v_{HO_2}}{4} \quad (4)$$

$$284 \quad v_{HO_2} = \sqrt{\frac{8 \times R \times T}{0.033 \times \Pi}} \quad (5)$$

285 Here, ASA represents the aerosol surface area [$\mu\text{m}^2 \text{cm}^{-3}$], which can be estimated
286 as 20 times the PM_{2.5} concentration [$\mu\text{g}/\text{cm}^3$]. v_{HO_2} [cm^{-1}] can be calculated using Eq.
287 (5), where T and R represent the temperature and gas constant, respectively. The
288 heterogeneous uptake coefficient (γ) for HO₂ usually has high uncertainty, with typical
289 values ranging from 0 to 1 (Song et al., 2021). In this study, we set γ to 0.08 to
290 evaluate the influence of HO₂ uptake on radical concentrations.

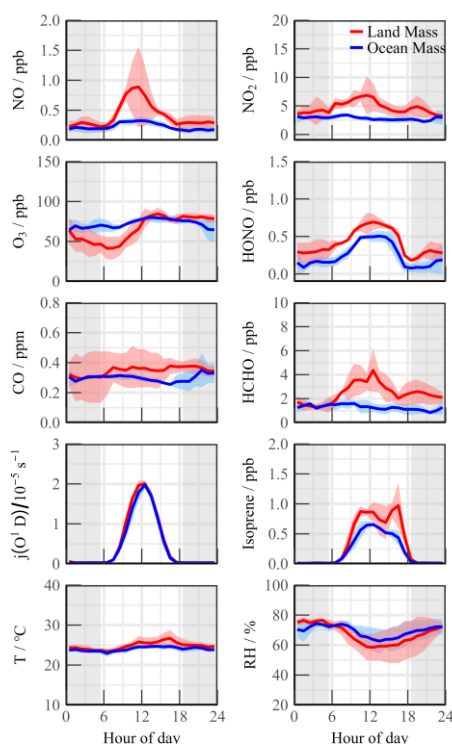
291 **3 Results**

292 **3.1 Meteorological and chemical parameters**

293 Fig. S3 presents the time series of the main meteorological parameters and
294 pollutants during the observation period at the YMK site. Except for on 2 days,
295 October 26 and 28, the meteorological characteristics of the other days were generally
296 stable. The daily maximum T, RH, and J-values did not vary significantly. The
297 suitable temperature (20–30°C) and humidity (40–80%) conditions promoted the
298 stable oxidation of the diurnal photochemistry. The peak $j(\text{O}^1\text{D})$ value was
299 approximately $2.0 \times 10^{-5} \text{ s}^{-1}$, exhibiting the typical characteristics of intense light
300 radiation in autumn in the Pearl River Delta region (Yang et al., 2022a; Tan et al.,
301 2022).

302 As typical marine air components, the concentrations of NO_x, CO, PM_{2.5}, and
303 other pollutants were lower than those detected in other observation campaigns in
304 both urban and suburban areas in the Pearl River Delta region (Tan et al., 2019b; Lu et

305 al., 2012; Yang et al., 2022b). Several observation campaigns have discovered the
 306 relationship between wind direction and radical chemistry (Lu et al., 2012; Fuchs et
 307 al., 2017; Niu et al., 2022). Although there was no apparent wind speed condition, the
 308 dominant air mass still influenced the pollutant concentrations due to the particularity
 309 of the marine site.



310
 311 **Fig. 2.** Mean diurnal profiles of measured trace gases parameters during Land mass and Ocean mass episodes. The
 312 coloured shadows denote the 25 and 75% percentiles. The grey areas denote nighttime.

313 During the OCM period, the NO_x and HCHO concentrations exhibited relatively
 314 clean characteristics that were consistent with those previously observations in open
 315 ocean (RHAMBLe, SOS, CHABLIS and ALBATROSS, Table 1). Isoprene, a
 316 representative BVOC, achieved a diurnal concentration of 0.58 ± 0.06 ppb, indicated
 317 slightly local emissions could have impacted the concentrations of the precursor
 318 species even in OCM sector. The ozone concentration in the YMK site was always at
 319 the critical value of the updated Class I standard (GB3095-2012, average hourly O₃ of
 320 81 ppb at 25°C and 1013 kPa). The occurrence of fewer emissions reduced the
 321 titration effect, resulting in the ozone exhibiting no apparent diurnal trend on some of
 322 the dates and a high background value at night (78.1 ± 7.6 ppb).

323 As a coastal site, chemical conditions could be influenced by local land emissions

324 depending on the wind direction. Compared with the OCM period, the meteorological
325 conditions (T, RH, and J-values) changed slightly during the LAM episode, but the
326 pollutants were accumulated due to the transport of the plume from the northern cities
327 (Fig. 2). The CO and PM_{2.5} concentrations exhibited good consistency and even mild
328 pollution features ((0.36 ± 0.12 ppm) and (37.70 ± 7.91 µg/m³), respectively),
329 reflecting the influence of human activities. Both NO and NO₂ peaked at around
330 10:00, exhibiting prominent pollution characteristics. HONO exhibited a distribution
331 with high daytime (0.66 ± 0.08 ppb) and low nighttime (0.33 ± 0.09 ppb)
332 concentrations. This unique distribution of HONO has been observed in remote
333 environments in several previous observation campaigns (Jiang et al., 2022; Crilley et
334 al., 2021). High HONO concentration in the daytime will affect the chemical
335 composition of the atmosphere and the secondary pollution generation.

336 **Table 1.** Summary of radical concentrations and related species concentrations at MBL. All data are listed as the
337 average in noontime (10:00~15:00).

Campaign	Location	Category	Date	OH (10 ⁶ cm ⁻³)	HO ₂ (10 ⁸ cm ⁻³)	HCHO (ppb)	HONO (ppb)	NO _x (ppb)	O ₃ (ppb)	Reference
WAOSE95	Weybourne, UK	Coastal	1995 (Jun)	5.0	-	1.50	0.10	<2.0	40.0	(Grenfell et al., 1999)
ALBATROSS	Atlantic Ocean	Open ocean	1996 (Oct-Nov)	7.0	-	0.50	-	-	25.0	(Brauers et al., 2001)
EASE96	Mace Head, Ireland	Coastal	1996 (Jul-Aug)	2.3	2.6	-	-	~1.0	45.0	(Carslaw et al., 1999)
EASE97	Mace Head, Ireland	Coastal	1997 (Apr-May)	1.8	1.0	0.70	-	0.95	46.0	(Creasey et al., 2002)
ORION99	Okinawa Island, Japan	Coastal	1999 (Aug)	4.0	4.3	-	0.20	6.3	23.0	(Kanaya et al., 2001)
RISOTTO	Rishiri Island, Japan	Coastal	2000 (June)	7.4	3.1	-	-	0.45	-	(Kanaya et al., 2002)
RISFEX	Rishiri Island, Japan	Coastal	2003 (Aug)	2.7	1.5	-	-	0.2	28.0	(Qi et al., 2007)
CHABLIS	Antarctica	Open ocean	2005 (Jan-Feb)	1.0	1.1	0.12	0.007	0.02	7.0	(Bloss et al., 2010)
RHaMBLe	Atlantic Ocean	Open ocean	2007 (May-Jun)	9.0	6.0	0.30	-	0.014	35.0	(Whalley et al., 2010)
SOS	Cape Verde, Atlantic Ocean	Open ocean	2009 (Jun; Sep)	9.0	4.0	1.9	-	0.050	40.0	(Carpenter et al., 2011)
CYPHEX	Cyprus, Mediterranean	Coastal	2014 (Jul)	5.8	6.3	~1.0	~0.080	<1.0	69.0	(Mallik et al., 2018)
ICOZA (NW-SE)	North Norfolk, UK	Coastal	2015 (Jul)	3.0	1.4	0.9	0.052	2.0	39.0	(Woodward-Massey et al., 2022b)
ICOZA (SW)	North Norfolk, UK	Coastal	2015 (Jul)	4.1	1.0	1.1	0.097	3.0	31.0	(Woodward-Massey et al., 2022b)
HT	Hok Tsui, China	Coastal	2020 (Oct-Nov)	4.9	-	1.0	0.15	~4.0	65.0	(Zou et al., 2022)

YMK (Land Mass)	Shenzhen, China	Coastal	2019 (Oct)	7.1	5.2	3.4	0.66	6.4	75.6	This work
YMK (Ocean Mass)	Shenzhen, China	Coastal	2019 (Oct)	4.5	4.9	1.2	0.48	3.0	78.1	This work

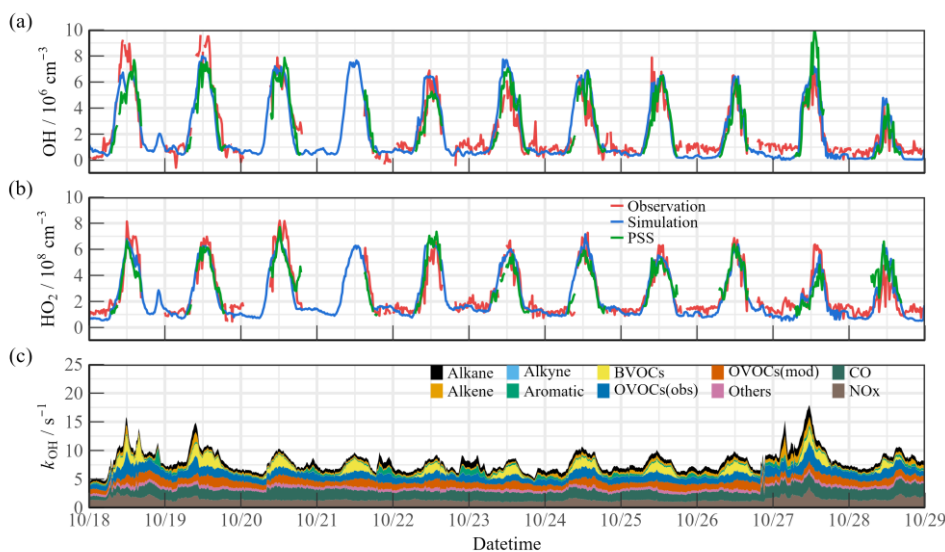
338

339 The detailed information for VOCs species during the YMK campaign has been
340 added in the Table S5. The daily maximum NMHC concentration peaked at $27.81 \pm$
341 9.91 ppb, and the maximum value of ~ 40 ppb occurred on October 27. Local
342 biological emissions significantly affected the NMHC composition of the site, and
343 isoprene achieved a noon maximum of 0.82 ± 0.16 ppb. Neither anthropogenic
344 alkenes (2.21 ± 0.94 ppb) nor aromatic (1.31 ± 0.25 ppb) hydrocarbons were abundant,
345 and OVOCs accounted for approximately 50% of the total. As a photochemical
346 indicator, formaldehyde peaked at ~ 4 to ~ 8 ppb during the LAM episode, suggesting a
347 more vigorous oxidation process. The HONO concentration was 6.8 times higher than
348 the SW scenario in the ICOZA observation (a pollution period dominated by a
349 southwest wind direction), while the HCHO concentration was 3.1 times higher.
350 (Woodward-Massey et al., 2022b). The abundance of oxidation precursors (HONO,
351 HCHO, O₃, and NMHCs) reflected the unique atmospheric conditions in the marine
352 environment in China, which originated from the complex atmospheric pollution.

353 **3.2 HO_x radical concentrations and modeled OH reactivity**

354 Fig. 3(a)(b) shows the time series of the simulated and observed OH and HO₂
355 radical concentrations during the observation campaign. The time series of the
356 simulated OH reactivity (k_{OH}) is presented in Fig. 3(c). The observed OH and HO₂
357 radicals exhibited significant diurnal trends. The daily maximum OH and HO₂ values
358 were $(4.7\text{--}9.5) \times 10^6 \text{ cm}^{-3}$ and $(4.2\text{--}8.1) \times 10^8 \text{ cm}^{-3}$, respectively. The peak k_{OH} value
359 was commonly less than 10 s^{-1} . Due to human activities, the simulated k_{OH} reached
360 more than $\sim 15 \text{ s}^{-1}$ on some days. The radical concentrations and reactivity exhibited
361 similar trends, which differed from reports on urban and semi-urban areas where
362 inorganic species (NO_x and CO) were the dominant controllers of k_{OH} (Zhang et al.,
363 2022a; Tan et al., 2019b; Lou et al., 2010). The k_{OVOCs} was separated into $k_{OVOCs(Obs)}$
364 and $k_{OVOCs(Model)}$ (Fig. 3(c)). Specifically, $k_{OVOCs(Obs)}$ includes the observed species

365 such as formaldehyde (HCHO), acetaldehyde (ACD), higher aldehydes (ALD),
 366 acetone (ACT), ketones (KET), and oxidation products of isoprene (MACR and
 367 MVK). The model-generated intermediates, such as glyoxal, methylglyoxal,
 368 methylethyl ketone, and methanol, are categorized as $k_{\text{OVOCs}(\text{Model})}$. Approximately 50%
 369 of the total k_{OVOCs} are represented by unconstrained species ($k_{\text{OVOCs}(\text{Model})}$), which
 370 contribute a daily k_{OH} of 1.39 s^{-1} . Overall, the observed OH and HO_2 concentrations
 371 were both well reproduced by the base model incorporating the RACM2-LIM1
 372 mechanism. The observed OH was underestimated only on the first days, and a slight
 373 model overestimation happened on October 23&24. PSS calculation showed good
 374 agreement with the base model, providing evidence of the balance of radical internal
 375 consistency in the daytime. It should be noted that the OH reactivity of unmeasured
 376 VOCs may be underestimated due to the lumped groups in RACM2 mechanism.

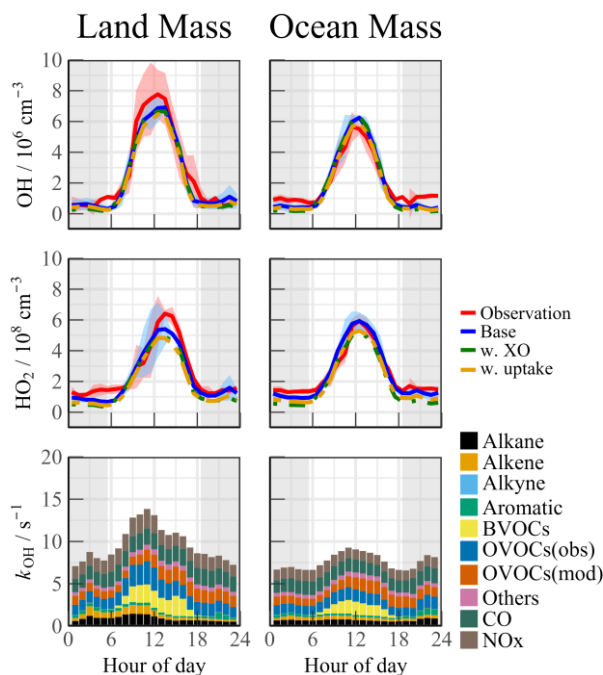


377
 378
 379

Fig. 3. Timeseries of the observed and modelled parameters for OH, HO_2 and k_{OH} during the observation period. (a) OH, (b) HO_2 , (c) k_{OH} .

380 The air mass transport of the precursors induced photochemistry accumulation,
 381 which was then reflected in the changes in the oxidation progress. It is worth
 382 comparing the concentrations and reactivities of the radicals by classifying the
 383 predominant air mass (Fig. 4). During the OCM period, the observed OH and HO_2
 384 radicals could be reflected by the base chemical mechanism, with daily averages of
 385 $4.5 \times 10^6 \text{ cm}^{-3}$ and $4.9 \times 10^8 \text{ cm}^{-3}$, respectively. Compared to other campaigns (Table
 386 1), the observed maximum values were within reasonable ranges (OH: $2 - 9 \times 10^6$

387 cm^{-3} ; HO_2 : $1 - 6 \times 10^8 \text{ cm}^{-3}$). Despite low NO_x levels during the OCM period, the
388 HO_2 radical was not overestimated using the base model, which was dissimilar to
389 many MBL observations (Bloss et al., 2010). However, both the OH and HO_2 radical
390 concentrations reached higher levels during the LAM-dominant period, indicating a
391 more active photochemical process (Section 4.1). The diel averages for the OH and
392 HO_2 radicals were $7.1 \times 10^6 \text{ cm}^{-3}$ and $5.2 \times 10^8 \text{ cm}^{-3}$, respectively, which were
393 notably higher than the levels reported in the ICOZA observations (Woodward-
394 Massey et al., 2022b). The base scenario underestimated both the OH and HO_2
395 concentrations between 10:00 and 15:00, and the observation-to-model ratio was
396 greater than 1.2. The calculated daily maximum total OH reactivity was 8.8 s^{-1} , and
397 nearly 70% of the reactivity was accounted for by the organic species, among which
398 the OVOCs were the largest contributor (30.6%). The anthropogenic alkanes, alkenes,
399 and aromatic hydrocarbons contributed less than 10% to the reactivity. Compared
400 with the OCM-dominant episode, the higher reactivity during the LAM period
401 indicated the occurrence of efficient recycling during the ROx (the sum of OH, HO_2 ,
402 and RO_2) propagation (12.4 s^{-1} vs. 8.8 s^{-1}). The higher contributions of the BVOCs
403 (only isoprene was considered, 15.6%) and OVOCs (30.2%) to the reactivity reflected
404 the diverse composition of the VOCs in the forest environment. Under enhanced
405 photochemistry, the calculated OH reactivity could be an underestimation of the total
406 OH reactivity, so a missing OH source may be masked. As a representative of the
407 OVOCs, HCHO reflects the photochemical level to a certain extent. As shown in Fig.
408 S5, a solid positive dependence between the $\text{OH}_{\text{obs-to-OH}_{\text{mod}}$ ratio and HCHO was
409 observed (the daytime data were restricted according to $j(\text{O}^1\text{D}) > 5 \times 10^{-6} \text{ s}^{-1}$). With
410 the increase of photochemical intensity, the ratio between the observed and simulated
411 OH radical showed an obvious mismatch. Obtaining the full magnitude of the radical-
412 related parameters is necessary to compensate for the discrepancy in the concentration
413 closure experiments.



414

415

416

417

Fig. 4. Median diurnal profiles of the observed and modelled OH, HO₂, k_{OH} during LAM and OCM episodes. The coloured shadows for OH and HO₂ radicals denote the 25 and 75% percentiles. The grey areas denote nighttime.

418

419

420

421

422

423

424

425

426

427

428

429

430

431

432

433

Halogen species have been recognized as potent oxidizers that can boost photochemistry (Xia et al., 2022; Peng et al., 2021). A sensitivity test was performed by imposing BrO and IO into the base model to diagnose the impact of the halogen chemistry on the troposphere chemistry. The concentration of BrO and IO is set to ~5 ppt, which is a typical level in MBL site (Xia et al., 2022; Bloss et al., 2010; Whalley et al., 2010). The details of the mechanisms involved are listed in Tables S3 and S4. In this scenario (Fig. 4, green line). The daytime concentration of HO₂ radical decreased by 8.5% and 13.3% during the LAM and OCM periods, respectively, compared to the base model. However, there was no significant change in the concentration of OH radicals (<3%). Traditionally, it is believed that the inclusion of halogen chemistry leads to higher modeled OH concentrations and lower modeled HO₂ concentrations. Therefore, the lack of an increase in OH concentration with the introduction of the halogen mechanism at the YMK site calls for further investigation (Fig. S6). By modifying the NO concentration in different levels (Scenario 1: [NO] × 150%, Scenario 2: base, Scenario 3: [NO] × 20%, Scenario 4: [NO] × 10%), the response of HO_x radicals to the halogen mechanism varied under different NO levels. As the

434 constrained NO increased from 30 ppt to 500 ppt, the reduction in HO₂ radicals due to
435 the Br and I mechanisms ranged between 10% and 20%. At elevated NO_x levels,
436 reactions between halogen radicals and NO_x occurred, inhibiting the formation of OH
437 radicals. In Scenario 1, the OH concentration even decreased by 3.5% when
438 introducing the halogen mechanism. When NO concentration was constrained around
439 30 ppt (Scenario 4), similar to those obtained in RHaMBLe/CYPHEX campaigns, the
440 modelled OH concentration increased by 14.4%, while the HO₂ concentration
441 decreased by approximately 20.8% (Whalley et al., 2010; Bloss et al., 2010).
442 Therefore, the sensitivity of OH radicals to the halogen mechanism in the YMK
443 region is primarily limited by the local NO_x concentration level.

444 Although the modelled and measured HO₂ showed good agreement, the effect of
445 HO₂ heterogeneous processes on the chemistry of HO_x radicals is also worth
446 exploring. The inclusion of heterogeneous processes ($\gamma = 0.08$) did reduce the
447 modelled HO₂ concentration for ~10% during both LAM and OCM periods (Fig. 4,
448 yellow line). This reduced agreement between observation and simulation emphasizes
449 the presence of a missing HO₂ source in the base model.

450 **4 Discussion**

451 **4.1 Experimental radical budget balance**

452 **4.1.1 OH radical**

453 A process-oriented experiment was conducted to investigate the photochemistry
454 progress from a budget balance perspective (Woodward-Massey et al., 2022a; Tan et
455 al., 2019b; Yang et al., 2021a). The OH was in a photostationary steady state due to its
456 short lifetime. The total OH removal rate was directly quantified from the union of the
457 OH concentration and the reactivity (Eq.(6)):

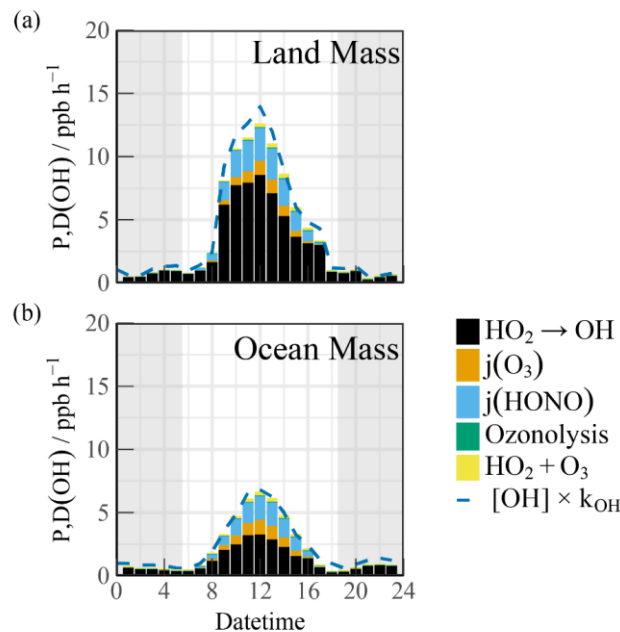
$$458 \quad D(OH) = [OH] \times k_{OH}. \quad (6)$$

459 The total production rate of the OH radical was the sum of the primary sources
460 (O₃/HONO photolysis and ozonolysis reactions) and secondary sources (HO₂ + NO)
461 (Eq.(7)):

$$\begin{aligned}
462 \quad P(OH) &= j_{HONO}[HONO] + \varphi_{OH}j(O^1D)[O_3] + \Sigma i \{ \varphi_{OH}^i k_{Alkenes+O_3}^i [Alkenes][O_3] \} \\
463 \quad &+ (k_{HO_2+NO}[NO] + k_{HO_2+O_3}[O_3])[HO_2]. \quad (7)
\end{aligned}$$

464 Here, φ_{OH} and φ_{OH}^i represent the OH yields in the O_3 photolysis and alkene
465 ozonolysis processes, respectively.

466 The diel profiles of the experimental OH budget during the LAM and OCM
467 periods are shown in Fig. 5. Both the observed OH and HO_2 radicals were introduced
468 into the budget calculations. Because k_{OH} was not measured during the observation
469 experiment, the simulated value was used to analyze the removal rate. Therefore,
470 $D(OH)$ should be considered a lower limit as it uses calculated rather than measured
471 k_{OH} (Yang et al., 2022b). During the OCM period, the $HO_2 + NO$ reaction accounted
472 for ~50% of the OH yield. The maximum of 6.6 ppb/h occurred at around 12:00. The
473 photolysis reactions could increase the daytime contributions of HONO and O_3 to
474 1.52 ppb/h and 0.84 ppb/h, respectively (10:00–15:00). The contribution of the non-
475 photolytic radical source (ozonolysis reactions) was almost negligible.



476 **Fig. 5.** The diurnal profiles of the experimental OH budget during (a) LAM and (b) OCM episodes. The blue
477 line denotes the OH destruction rate($[OH] \times k_{OH}$). The grey areas denote nighttime.
478

479 Compared with other marine observations, the calculated OH generation rate was
480 approximately twice that reported in the ICOZA and five times that obtained in the
481 RHaMBLe campaigns (Woodward-Massey et al., 2022a; Whalley et al., 2010).

482 During the LAM period, the OH generation rate reached a maximum of 12.6 ppb/h,
483 accompanied by a secondary source contribution of 67% (from the reaction between
484 HO₂ and NO) during the daytime, which was close to several observations related to
485 polluted plumes (Woodward-Massey et al., 2022a; Tan et al., 2019b; Lu et al., 2012;
486 Yang et al., 2022b). When the simulated k_{OH} was introduced into the experimental
487 budgets, the difference between P(OH) and D(OH) was less than 2 ppb/h.

488 **4.1.2 Total ROx radicals**

489 The budget analysis of the HO₂ and RO₂ radicals could not be performed well
490 due to the lack of RO₂ radical observation data. The diurnal profiles of the ROx
491 production (P(ROx)) and termination rate (L(ROx)) for the different air masses are
492 shown in Fig. 6. The P(ROx) could reach 3.36 ppb /h with an ocean plume. HONO
493 photolysis controlled nearly half of the primary sources (45.7%), and the daily
494 distribution was consistent with that of solar radiation. The ozone-related
495 contributions from photolysis and ozonolysis were approximately 46.6% (25.1% from
496 photolysis and 11.5% from ozonolysis, respectively). The remaining contribution was
497 from the photolysis of carbonyls (HCHO and OVOCs) (15.0%). The anthropogenic
498 contribution to the radical chemistry was not ignorable, and the ROx source in this
499 observation was exponentially higher than that in other MBL observations
500 (Woodward-Massey et al., 2022a; Stone et al., 2012; Whalley et al., 2010; Mallik et
501 al., 2018). The P(ROx) of the LAM was close to that in Shenzhen (~4 ppb/h) but was
502 significantly lower than that in Yufa (~7 ppb/h) and the BackGarden (~11 ppb/h) (Tan
503 et al., 2019b; Lu et al., 2012; Yang et al., 2022b). The reactions between ROx and
504 NOx and self-combination were the main pathways of radical termination (~70%).
505 The contribution of the formation of peroxyxynitrate to the L(ROx) could not be ignored
506 in the daytime.

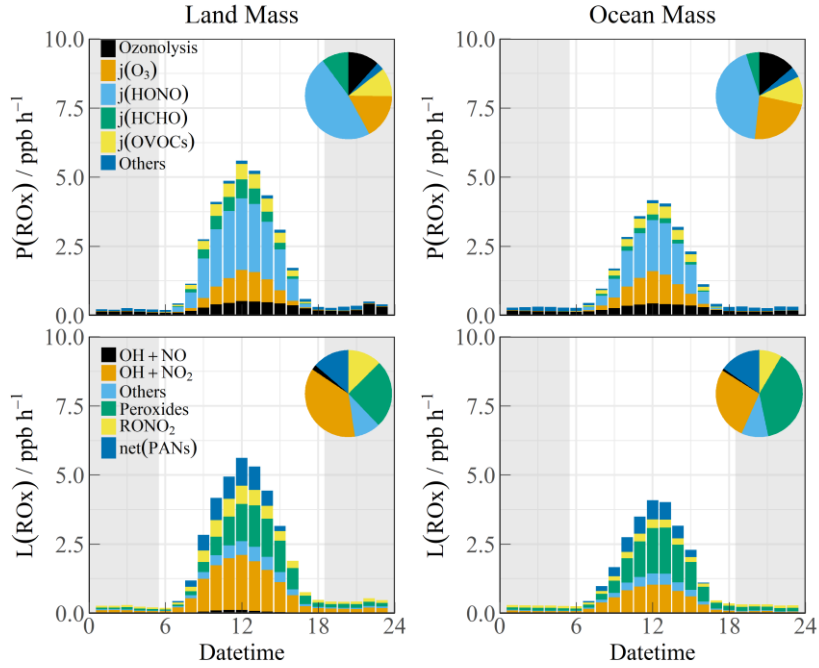


Fig. 6. The diurnal profiles of ROx budget during Land mass and Ocean mass episodes. The pie chart denotes proportions in different parts during the daytime (10:00-15:00). The grey areas denote nighttime.

The high daytime HONO concentrations observed at the YMK site is a notable phenomenon. Due to the high HONO concentration during the daytime, the photolysis reaction made daytime contributions of 1.52 ppb/h and 2.19 ppb/h during the OCM and LAM periods, respectively. As the only known gas-phase source, OH + NO accounted for a negligible proportion of the HONO production rate. Given the location of the site, HONO from cruise ship emissions is a possible component of the primary anthropogenic source (Sun et al., 2020). Other active tropospheric HONO sources (heterogeneous reactions with NO₂ and $p(NO_3^-)$ photolysis) are worthy of consideration and significantly contribute to the atmospheric oxidation in the MBL area (Zhu et al., 2022; Crilley et al., 2021).

4.2 Local ozone production rate

Peroxy radical chemistry is the essential photochemical source of tropospheric ozone ($F(O_x)$, Eq.(8)):

$$F(O_x) = k_{HO_2+NO}[NO][HO_2] + \sum_i (1 - \alpha_i) k_{RO_2^i+NO}[NO]RO_2^i \quad (8)$$

NO reacts with HO₂ and RO₂ radicals to form NO₂, and then, photolysis occurs to form O₃ under solar radiation. NO₂ and ozone are the two sides of the oxidation reservoir. The effect of local emissions on the photodynamic equilibrium can be avoided by characterizing the photochemical production of the total oxidants (Tan et

528 al., 2019b). α_i represents the organic nitrate yield, which affects the amount of NO_2
 529 that is produced from the reaction between RO_2 and NO (Tan et al., 2018b). Ox is
 530 mainly photochemically removed through ozone photolysis, ozonolysis, radical chain
 531 propagation ($\text{OH}/\text{HO}_2 + \text{O}_3$), and chain termination ($\text{OH} + \text{NO}_2$) reactions in the
 532 troposphere ($D(\text{Ox})$, Eq.(9)):

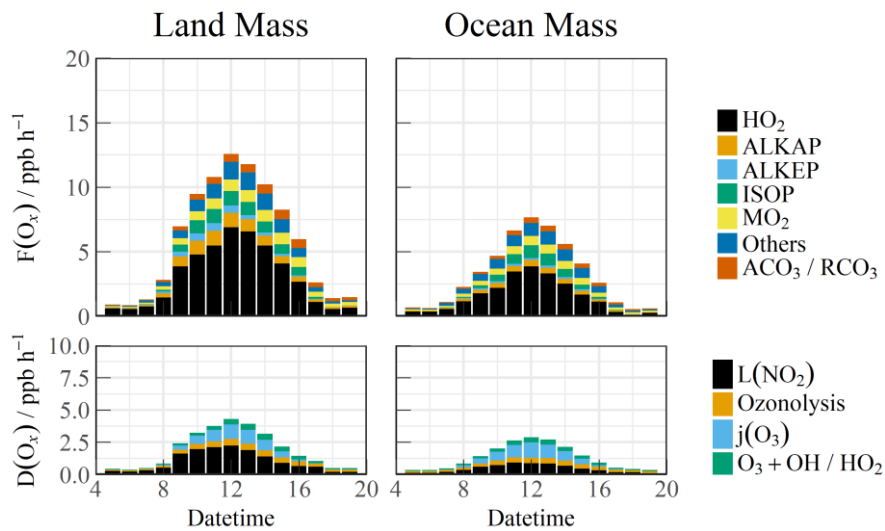
$$533 \quad D(\text{O}_x) = \varphi_{\text{OH}} j(\text{O}^1\text{D})[\text{O}_3] + \Sigma i \{k_{\text{Alkenes}+\text{O}_3}^i [\text{Alkenes}][\text{O}_3]\} + (k_{\text{O}_3+\text{OH}}[\text{OH}] +$$

$$534 \quad k_{\text{O}_3+\text{HO}_2}[\text{HO}_2][\text{O}_3] + k_{\text{OH}+\text{NO}_2}[\text{OH}][\text{NO}_2]) \quad (9)$$

535 The net formation rate $P(\text{O}_x)$ can be calculated by subtracting $D(\text{O}_x)$ from $F(\text{O}_x)$
 536 (Eq.(10)):

$$537 \quad P(\text{O}_x) = F(\text{O}_x) - D(\text{O}_x) \quad (10)$$

538 The simulated RO_2 radical concentration was introduced into the $F(\text{O}_x)$
 539 calculation. The diurnal variations in the ozone generation in the different air masses
 540 are shown in Fig. 7. The contribution of the HO_2 radical to $F(\text{O}_x)$ was approximately
 541 60%. The RO_2 radicals consisted of various types such as methyl peroxy (MO_2),
 542 acetyl peroxy radicals ($\text{ACO}_3/\text{RCO}_3$), and other radicals derived from alkanes
 543 (ALKAP), alkenes (ALKEP), and isoprene (ISOP), which accounted for an additional
 544 40% of the $F(\text{O}_x)$. On a daytime basis, the maximum $F(\text{O}_x)$ reached 7.4 ppb/h at
 545 around 12:00 in the OCM period, while a persistent-high value (maximum of 12.5
 546 ppb/h at 10:00–14:00) occurred in the LAM period. A vast amount of Ox was
 547 consumed in the nitric acid ($\text{OH} + \text{NO}_2$) formation pathways, i.e., higher than the
 548 ozonolysis removal. The daily averaged ozone production rates were 5.52 and 2.76
 549 ppb/h during the LAM and OCM periods, respectively.



550

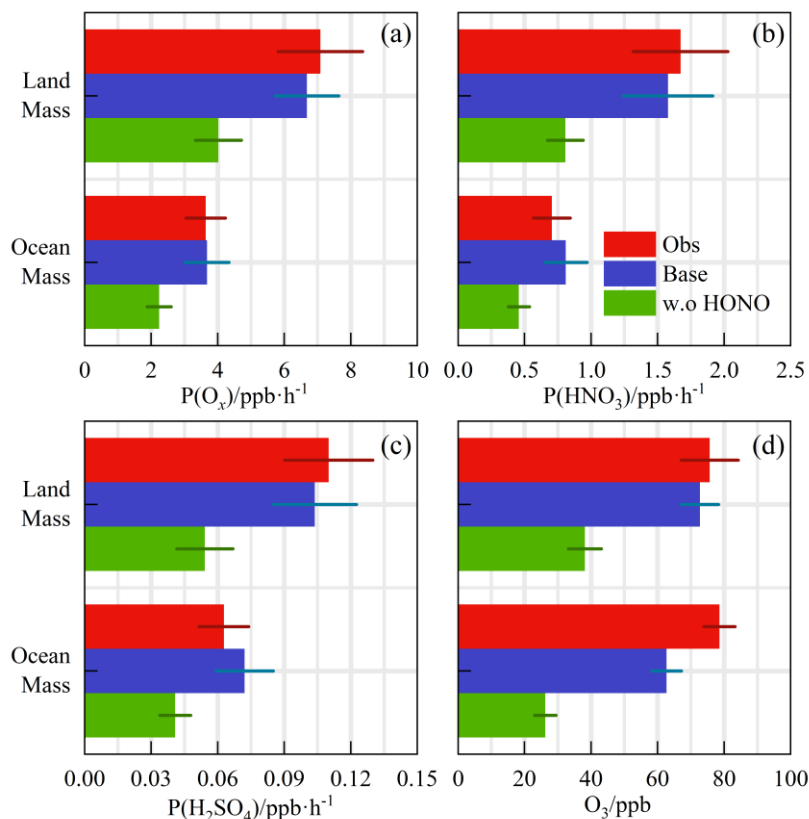
551 **Fig. 7.** The diurnal profiles of the speciation F(O_x) and D(O_x) during Land mass and Ocean mass episodes.
552 The data were calculated by the measured OH and HO₂ and modelled RO₂ radicals.

553 **4.3 Relationship between precursors and oxidation rates**

554 Despite the low level of human activities, oxidation precursors have an extended
555 lifetime in the stable atmosphere of coastal areas. Intensive photochemical reactions
556 occur after the accumulation of precursors, resulting in local net ozone production
557 comparable to that in the surrounding suburban environments (Zeren et al., 2022).
558 Simultaneous observations of both urban and coastal settings in Shenzhen have
559 indicated that the oxidation rates are comparable (Xia et al., 2021). The coupling of
560 precursor transport and local photochemical processes in marine areas makes it
561 meaningful to explore secondary pollution generation (Fig. 8(a), (b), and (c)). No
562 obvious radical source was missing during the LAM and OCM periods, and the
563 oxidation level was that expected from the base model. On a daytime basis, the mean
564 diurnal profile of the P(O_x) reached ~7 ppb/h in the LAM period, and the average
565 nitric acid (P(HNO₃)) and sulfuric acid (P(H₂SO₄)) production rates were ~1.6 and
566 ~0.11 ppb/h, respectively. The P(HNO₃) production rate was similar to the average of
567 observations in the Pearl River Delta region (~1.3 ppb/h), while that of the P(H₂SO₄)
568 was only half the average level (~0.24 ppb/h) (Lu et al., 2013; Tan et al., 2019b; Yang
569 et al., 2022b). During the OCM period, the characteristics of the ocean air mass
570 alleviated the photochemical process, and the production rates of the secondary
571 pollutants decreased by approximately half and were close to the average levels in
572 winter (Ma et al., 2019).

573 Contrary to numerous ocean observations, in the YMK site, intensive oxidation
574 was accompanied by a high diurnal HONO level (higher than 400 ppt) (Fig. 9). The
575 ozone levels were consistent with the Grade I air quality standard and far exceeded
576 the global background concentration (~40 ppb). Daytime photolysis reactions of
577 HONO contributed 1.52 ppb/h and 2.19 ppb/h to P(RO_x) during the OCM and LAM
578 periods, respectively, which were much higher than the values in several megacities
579 during the photochemically polluted season (Tan et al., 2019a). Given the significance
580 of HONO photolysis in driving atmospheric chemistry, a sensitivity test was

581 conducted without constraints on HONO (i.e., w.o HONO) to specifically quantify the
 582 contribution of HONO-induced secondary pollution. Only the homogeneous reaction
 583 (OH + NO) participated in the formation of HONO in the default mode without
 584 HONO input (Liu et al., 2022b).



585
 586 **Fig. 8.** The calculated reaction rates based on the observed concentrations for Land mass and Ocean mass
 587 episodes (a) $P(O_x)$, (b) $P(HNO_3)$, (c) $P(H_2SO_4)$. (d) The observed and modelled O_3 concentration with a first-order
 588 loss term. The deposition process was equivalent to a lifetime of 15 hours to all species. All the rates and
 589 concentration are averaged for the daytime period between 10:00 and 15:00.

590 The modelled OH, HO_2 and RO_2 change when the model was unconstrained to
 591 HONO were shown in Fig. S7. After evaluation, in LAM and OCM sectors,
 592 concentration changes for OH were 46.9% and 43.2%, for HO_2 were 38.3% and
 593 34.3%, for RO_2 were 43.7% and 39.0%, respectively. The $P(O_x)$ was found to be 33%
 594 and 39% lower during the LAM and OCM periods, respectively. The nitric acid
 595 ($P(HNO_3)$) and sulfuric acid ($P(H_2SO_4)$) formation rates also increased
 596 simultaneously (~43% and ~48% for LAM and OCM sectors, respectively). The
 597 sensitivity test identified the privileged role of the HONO-related mechanisms in the
 598 OH chemistry, which resulted in a correlation between the efficient radical recycling
 599 and secondary pollution.

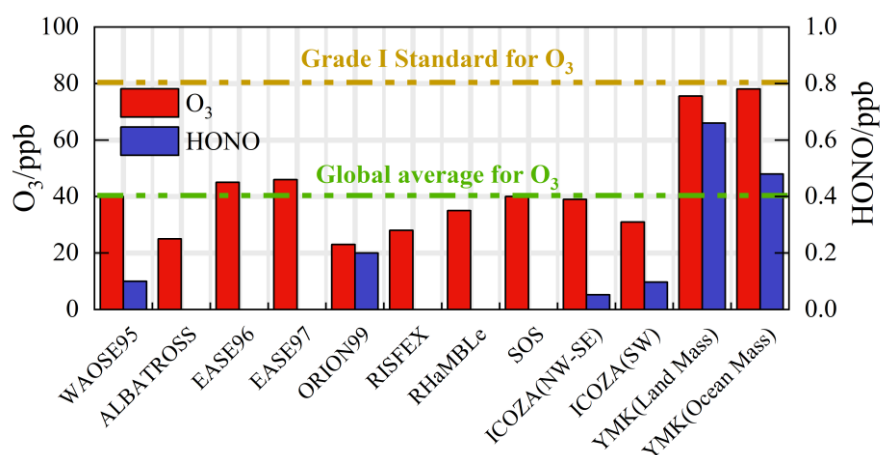


Fig. 9. Summary of both ozone and HONO concentrations in previous marine observations. The concentrations are averaged for the daytime period between 10:00 and 15:00.

600
601
602

603 A time-dependent box model was used to test the association between the HONO
604 chemistry and the local ozone generation (Fig. 8(d)). In order to isolate the O₃
605 photochemical production, the impacts of vertical entrainment and horizontal
606 advection were in general ignored. Comparatively, removing the constraints on ozone
607 and NO while keeping NO₂ as a constraint is a commonly used method in the box
608 model for ozone prediction (Tan et al., 2018a). Considering the complexity of HONO
609 chemistry, we emphasize that this is a sensitivity test for ozone prediction, and its
610 validity has been examined through simulated comparisons under different HONO
611 concentrations (Fig. S8). The observed and modelled O₃ concentrations in Fig. 8(d)
612 are averaged for the daytime period between 10:00 and 15:00. The observed diurnal
613 ozone concentrations were 75.7 ppb and 78.6 ppb during the LAM and OCM periods,
614 respectively. The daytime ozone was well reproduced by the time-dependent box
615 model, and the deviation of the simulation was less than 20% (Fig. 8(d)). After
616 removing the HONO constraint, the simulated ozone concentrations were 38.2 and
617 26.3 ppb, i.e., 48% and 58% lower, during the LAM and OCM periods, respectively.
618 Simulated O₃ decreased from ~75 ppb to a global background, and daytime HONO
619 concentration were reduced to a low level (~70 ppt) (Woodward-Massey et al., 2022b;
620 Zhu et al., 2022; Xia et al., 2022). The elevated daytime HONO had an additional
621 effect on the oxidation in the background atmosphere. For coastal cities, the
622 particularity of the HONO chemistry in the MBL tends to influence the ozone-
623 sensitive system and eventually magnifies the ozone background. Therefore, the

624 promotion of oxidation by elevated precursor concentrations is worth considering
625 when formulating emission reduction policies. In regions where HONO
626 concentrations are elevated, the sources of HONO would need to be identified to aid
627 pollution mitigation policies.

628 **5 Conclusions**

629 Comprehensive observations of HOx radicals and other relevant species were
630 conducted in October 2019 at a coastal site in the Pearl River Delta (the YMK site,
631 22.55°N, 114.60°E). The overall air pollutants exhibited typical coastal features due to
632 the scarce anthropogenic emissions. The daily maximum OH and HO₂ concentrations
633 were $(4.7\text{--}9.5) \times 10^6 \text{ cm}^{-3}$ and $(4.2\text{--}8.1) \times 10^8 \text{ cm}^{-3}$, respectively. The base RACM2-
634 LIM1 model satisfactorily reproduced both the observed OH and HO₂ radical
635 concentrations, but a slight overestimation of the OH radical occurred. The daily
636 maximum calculated total OH reactivity was 9.9 s^{-1} , and nearly 70% of the reactivity
637 was contributed by organic species.

638 In addition to anthropogenic and vegetation emissions, the synchronized air mass
639 transport from the northern cities and the South China Sea exerted a time-varying
640 influence on radical photochemistry and atmospheric oxidation. During the OCM
641 period, the observed OH and HO₂ radical concentrations could be reflected by the
642 base chemical mechanism, with daily average values of $4.5 \times 10^6 \text{ cm}^{-3}$ and 4.9×10^8
643 cm^{-3} , respectively.

644 In the episode that was dominated by ocean mass, the HO₂ + NO reaction
645 accounted for ~50% of the primary OH yield. A higher OH generation rate was
646 found (12.6 ppb/h) during the LAM period, and the secondary source accounted for 67%
647 of the total, which was similar to several observations in polluted plumes. Reactions
648 between ROx and NOx and self-combination were the main pathways of radical
649 termination (~70%), and the contribution of peroxyxynitrate formation to the L(ROx)
650 could not be ignored in the daytime.

651 Intensive photochemical reactions occur after the accumulation of precursors,

652 resulting in local net ozone production comparable to that in the surrounding suburban
653 environments. The daily average ozone production rates were 5.52 and 2.76 ppb/h in
654 the LAM and OCM periods, respectively. The rapid oxidation process was
655 accompanied by a higher diurnal HONO concentration (higher than 400 ppt). A non-
656 HONO-constrained sensitivity test was performed to quantify the HONO-induced
657 contribution to secondary pollution. After evaluation, the P(Ox) values were 33% and
658 39% lower during the LAM and OCM periods, respectively. The nitric acid (P(HNO₃))
659 and sulfuric acid (P(H₂SO₄)) formation rates also increased simultaneously (~43%
660 and ~48% for LAM and OCM sectors, respectively). Simulated O₃ decreased from
661 ~75 ppb to a global background, and daytime HONO concentration were reduced to a
662 low level (~70 ppt). For coastal cities, the particularity of the HONO chemistry in the
663 MBL tends to influence the ozone-sensitive system and eventually magnifies the
664 ozone background. Therefore, the promotion of oxidation by elevated precursor
665 concentrations is worth considering when formulating emission reduction policies.

666 **Financial support**

667 This work was supported by the National Natural Science Foundation of China
668 (62275250, U19A2044, 61905003), the Natural Science Foundation of Anhui
669 Province (No. 2008085J20), the National Key R&D Program of China
670 (2022YFC3700301), and the Anhui Provincial Key R&D Program (2022107020022).

671 **Data availability**

672 The data used in this study are available from the corresponding author upon request
673 (rzhu@aiofm.ac.cn).

674 **Author contributions**

675 WQ Liu, PH Xie, RZ Hu contributed to the conception of this study. GX Zhang and
676 RZ Hu performed the data analyses and manuscript writing. All authors contributed to
677 measurements, discussed results, and commented on the paper.

678 **Competing interests**

679 The contact author has declared that none of the authors has any competing interests.

680

681

References

- 683 Bloss, W. J., Camredon, M., Lee, J. D., Heard, D. E., Plane, J. M. C., Saiz-Lopez, A., Bauguitte, S. J. B.,
684 Salmon, R. A., and Jones, A. E.: Coupling of HO_x, NO_x and halogen chemistry in the antarctic
685 boundary layer, *Atmos Chem Phys*, 10, 10187-10209, 10.5194/acp-10-10187-2010, 2010.
- 686 Brauers, T., Hausmann, M., Bister, A., Kraus, A., and Dorn, H.-P.: OH radicals in the boundary layer of
687 the Atlantic Ocean: 1. Measurements by long-path laser absorption spectroscopy, *Journal of*
688 *Geophysical Research*, 106, 7399, 10.1029/2000jd900679, 2001.
- 689 Carpenter, L. J., Fleming, Z. L., Read, K. A., Lee, J. D., Moller, S. J., Hopkins, J. R., Purvis, R. M.,
690 Lewis, A. C., Müller, K., Heinold, B., Herrmann, H., Fomba, K. W., van Pinxteren, D., Müller, C.,
691 Tegen, I., Wiedensohler, A., Müller, T., Niedermeier, N., Achterberg, E. P., Patey, M. D., Kozlova, E. A.,
692 Heimann, M., Heard, D. E., Plane, J. M. C., Mahajan, A., Oetjen, H., Ingham, T., Stone, D., Whalley, L.
693 K., Evans, M. J., Pilling, M. J., Leigh, R. J., Monks, P. S., Karunaharan, A., Vaughan, S., Arnold, S. R.,
694 Tschritter, J., Pöhler, D., Friß, U., Holla, R., Mendes, L. M., Lopez, H., Faria, B., Manning, A. J., and
695 Wallace, D. W. R.: Seasonal characteristics of tropical marine boundary layer air measured at the Cape
696 Verde Atmospheric Observatory, *J Atmos Chem*, 67, 87-140, 10.1007/s10874-011-9206-1, 2011.
- 697 Carslaw, N., Creasey, D. J., Heard, D. E., Lewis, A. C., McQuaid, J. B., Pilling, M. J., Monks, P. S.,
698 Bandy, B. J., and Penkett, S. A.: Modeling OH, HO₂, and RO₂ radicals in the marine boundary layer: 1.
699 Model construction and comparison with field measurements, *Journal of Geophysical Research:*
700 *Atmospheres*, 104, 30241-30255, 10.1029/1999jd900783, 1999.
- 701 Chen, W., Guenther, A. B., Shao, M., Yuan, B., Jia, S., Mao, J., Yan, F., Krishnan, P., and Wang, X.:
702 Assessment of background ozone concentrations in China and implications for using region-specific
703 volatile organic compounds emission abatement to mitigate air pollution, *Environ Pollut*, 305, 119254,
704 10.1016/j.envpol.2022.119254, 2022.
- 705 Creasey, D. J., Heard, D. E., and Lee, J. D.: Eastern Atlantic Spring Experiment 1997 (EASE97) 1.
706 Measurements of OH and HO₂ concentrations at Mace Head, Ireland, *Journal of Geophysical Research:*
707 *Atmospheres*, 107, ACH 3-1-ACH 3-15, 10.1029/2001jd000892, 2002.
- 708 Crilley, L. R., Kramer, L. J., Pope, F. D., Reed, C., Lee, J. D., Carpenter, L. J., Hollis, L. D. J., Ball, S.
709 M., and Bloss, W. J.: Is the ocean surface a source of nitrous acid (HONO) in the marine boundary
710 layer?, *Atmos Chem Phys*, 21, 18213-18225, 10.5194/acp-21-18213-2021, 2021.
- 711 Fuchs, H., Dorn, H. P., Bachner, M., Bohn, B., Brauers, T., Gomm, S., Hofzumahaus, A., Holland, F.,
712 Nehr, S., Rohrer, F., Tillmann, R., and Wahner, A.: Comparison of OH concentration measurements by
713 DOAS and LIF during SAPHIR chamber experiments at high OH reactivity and low NO concentration,
714 *Atmos Meas Tech*, 5, 1611-1626, 10.5194/amt-5-1611-2012, 2012.
- 715 Fuchs, H., Tan, Z., Lu, K., Bohn, B., Broch, S., Brown, S. S., Dong, H., Gomm, S., Haeseler, R., He, L.,
716 Hofzumahaus, A., Holland, F., Li, X., Liu, Y., Lu, S., Min, K.-E., Rohrer, F., Shao, M., Wang, B., Wang,
717 M., Wu, Y., Zeng, L., Zhang, Y., Wahner, A., and Zhang, Y.: OH reactivity at a rural site (Wangdu) in
718 the North China Plain: contributions from OH reactants and experimental OH budget, *Atmos Chem*
719 *Phys*, 17, 645-661, 10.5194/acp-17-645-2017, 2017.
- 720 Grenfell, J. L., Savage, N. H., Harrison, R. M., Penkett, S. A., Forberich, O., Comes, F. J., Clemitshaw,
721 K. C., Burgess, R. A., Cardenas, L. M., Davison, B., and McFadyen, G. G.: Tropospheric box-
722 modelling and analytical studies of the hydroxyl (OH) radical and related species: Comparison with
723 observations, *J Atmos Chem*, 33, 183-214, 10.1023/a:1006009901180, 1999.

724 Griffith, S. M., Hansen, R. F., Dusanter, S., Stevens, P. S., Alaghmand, M., Bertman, S. B., Carroll, M.
725 A., Erickson, M., Galloway, M., Grossberg, N., Hottle, J., Hou, J., Jobson, B. T., Kammrath, A.,
726 Keutsch, F. N., Lefer, B. L., Mielke, L. H., O'Brien, A., Shepson, P. B., Thurlow, M., Wallace, W.,
727 Zhang, N., and Zhou, X. L.: OH and HO₂ radical chemistry during PROPHET 2008 and CABINEX
728 2009-Part 1: Measurements and model comparison, *Atmos Chem Phys*, 13, 5403-5423, 10.5194/acp-
729 13-5403-2013, 2013.

730 Huang, R. J., Hoffmann, T., Ovadnevaite, J., Laaksonen, A., Kokkola, H., Xu, W., Xu, W., Ceburnis, D.,
731 Zhang, R., Seinfeld, J. H., and O'Dowd, C.: Heterogeneous iodine-organic chemistry fast-tracks marine
732 new particle formation, *Proc Natl Acad Sci U S A*, 119, e2201729119, 10.1073/pnas.2201729119, 2022.

733 Jiang, Y., Xue, L., Shen, H., Dong, C., Xiao, Z., and Wang, W.: Dominant Processes of HONO Derived
734 from Multiple Field Observations in Contrasting Environments, *Environmental Science & Technology*
735 *Letters*, 10.1021/acs.estlett.2c00004, 2022.

736 Kanaya, Y., Sadanaga, Y., Nakamura, K., and Akimoto, H.: Behavior of OH and HO₂ radicals during
737 the Observations at a Remote Island of Okinawa (ORION99) field campaign 1. Observation using a
738 laser-induced fluorescence instrument, *J Geophys Res-Atmos*, 106, 24197-24208,
739 10.1029/2000jd000178, 2001.

740 Kanaya, Y., Yokouchi, Y., Matsumoto, J., Nakamura, K., Kato, S., Tanimoto, H., Furutani, H., Toyota,
741 K., and Akimoto, H.: Implications of iodine chemistry for daytime HO₂ levels at Rishiri Island,
742 *Geophys Res Lett*, 29, 45-41-45-44, 10.1029/2001gl014061, 2002.

743 Liu, C., Liu, G., Casazza, M., Yan, N., Xu, L., Hao, Y., Franzese, P. P., and Yang, Z.: Current Status and
744 Potential Assessment of China's Ocean Carbon Sinks, *Environ Sci Technol*, 56, 6584-6595,
745 10.1021/acs.est.1c08106, 2022a.

746 Liu, P., Xue, C., Ye, C., Liu, C., Zhang, C., Wang, J., Zhang, Y., Liu, J., and Mu, Y.: The Lack of
747 HONO Measurement May Affect the Accurate Diagnosis of Ozone Production Sensitivity, *ACS*
748 *Environmental Au*, 10.1021/acsenvironau.2c00048, 2022b.

749 Liu, T., Hong, Y., Li, M., Xu, L., Chen, J., Bian, Y., Yang, C., Dan, Y., Zhang, Y., Xue, L., Zhao, M.,
750 Huang, Z., and Wang, H.: Atmospheric oxidation capacity and ozone pollution mechanism in a coastal
751 city of southeastern China: analysis of a typical photochemical episode by an observation-based model,
752 *Atmos Chem Phys*, 22, 2173-2190, 10.5194/acp-22-2173-2022, 2022c.

753 Lou, S., Holland, F., Rohrer, F., Lu, K., Bohn, B., Brauers, T., Chang, C. C., Fuchs, H., Haseler, R.,
754 Kita, K., Kondo, Y., Li, X., Shao, M., Zeng, L., Wahner, A., Zhang, Y., Wang, W., and Hofzumahaus, A.:
755 Atmospheric OH reactivities in the Pearl River Delta – China in summer 2006: measurement and
756 model results, *Atmos Chem Phys*, 10, 11243–11260, 10.5194/acp-10-11243-2010, 2010.

757 Lu, K. D., Guo, S., Tan, Z. F., Wang, H. C., Shang, D. J., Liu, Y. H., Li, X., Wu, Z. J., Hu, M., and
758 Zhang, Y. H.: Exploring atmospheric free-radical chemistry in China: the self-cleansing capacity and
759 the formation of secondary air pollution, *Natl. Sci. Rev.*, 6, 579-594, 10.1093/nsr/nwy073, 2019.

760 Lu, K. D., Hofzumahaus, A., Holland, F., Bohn, B., Brauers, T., Fuchs, H., Hu, M., Haeseler, R., Kita,
761 K., Kondo, Y., Li, X., Lou, S. R., Oebel, A., Shao, M., Zeng, L. M., Wahner, A., Zhu, T., Zhang, Y. H.,
762 and Rohrer, F.: Missing OH source in a suburban environment near Beijing: observed and modelled
763 OH and HO₂ concentrations in summer 2006, *Atmos Chem Phys*, 13, 1057-1080, 10.5194/acp-13-
764 1057-2013, 2013.

765 Lu, K. D., Rohrer, F., Holland, F., Fuchs, H., Bohn, B., Brauers, T., Chang, C. C., Haeseler, R., Hu, M.,
766 Kita, K., Kondo, Y., Li, X., Lou, S. R., Nehr, S., Shao, M., Zeng, L. M., Wahner, A., Zhang, Y. H., and
767 Hofzumahaus, A.: Observation and modelling of OH and HO₂ concentrations in the Pearl River Delta

768 2006: a missing OH source in a VOC rich atmosphere, *Atmos Chem Phys*, 12, 1541-1569,
769 10.5194/acp-12-1541-2012, 2012.

770 Ma, X. F., Tan, Z. F., Lu, K. D., Yang, X. P., Liu, Y. H., Li, S. L., Li, X., Chen, S. Y., Novelli, A., Cho,
771 C. M., Zeng, L. M., Wahner, A., and Zhang, Y. H.: Winter photochemistry in Beijing: Observation and
772 model simulation of OH and HO₂ radicals at an urban site, *Sci Total Environ*, 685, 85-95,
773 10.1016/j.scitotenv.2019.05.329, 2019.

774 Mallik, C., Tomsche, L., Bourtsoukidis, E., Crowley, J. N., Derstroff, B., Fischer, H., Hafermann, S.,
775 Hüser, I., Javed, U., Keßel, S., Lelieveld, J., Martinez, M., Meusel, H., Novelli, A., Phillips, G. J.,
776 Pozzer, A., Reiffs, A., Sander, R., Taraborrelli, D., Sauvage, C., Schuladen, J., Su, H., Williams, J., and
777 Harder, H.: Oxidation processes in the eastern Mediterranean atmosphere: evidence from the modelling
778 of HO_x; measurements over Cyprus, *Atmos Chem Phys*, 18, 10825-10847, 10.5194/acp-18-10825-
779 2018, 2018.

780 Niu, Y. B., Zhu, B., He, L. Y., Wang, Z., Lin, X. Y., Tang, M. X., and Huang, X. F.: Fast Nocturnal
781 Heterogeneous Chemistry in a Coastal Background Atmosphere and Its Implications for Daytime
782 Photochemistry, *Journal of Geophysical Research: Atmospheres*, 127, 10.1029/2022jd036716, 2022.

783 Peng, X., Wang, W. H., Xia, M., Chen, H., Ravishankara, A. R., Li, Q. Y., Saiz-Lopez, A., Liu, P. F.,
784 Zhang, F., Zhang, C. L., Xue, L. K., Wang, X. F., George, C., Wang, J. H., Mu, Y. J., Chen, J. M., and
785 Wang, T.: An unexpected large continental source of reactive bromine and chlorine with significant
786 impact on wintertime air quality, *Natl. Sci. Rev.*, 8, 10.1093/nsr/nwaa304, 2021.

787 Qi, B., Kanaya, Y., Takami, A., Hatakeyama, S., Kato, S., Sadanaga, Y., Tanimoto, H., and Kajii, Y.:
788 Diurnal peroxy radical chemistry at a remote coastal site over the sea of Japan, *Journal of Geophysical*
789 *Research*, 112, 10.1029/2006jd008236, 2007.

790 Slater, E. J., Whalley, L. K., Woodward-Massey, R., Ye, C., Lee, J. D., Squires, F., Hopkins, J. R.,
791 Dunmore, R. E., Shaw, M., Hamilton, J. F., Lewis, A. C., Crilley, L. R., Kramer, L., Bloss, W., Vu, T.,
792 Sun, Y., Xu, W., Yue, S., Ren, L., Acton, W. J. F., Hewitt, C. N., Wang, X., Fu, P., and Heard, D. E.:
793 Elevated levels of OH observed in haze events during wintertime in central Beijing, *Atmos Chem Phys*,
794 20, 14847-14871, 10.5194/acp-20-14847-2020, 2020.

795 Song, H., Lu, K., Dong, H., Tan, Z., Chen, S., Zeng, L., and Zhang, Y.: Reduced Aerosol Uptake of
796 Hydroperoxyl Radical May Increase the Sensitivity of Ozone Production to Volatile Organic
797 Compounds, *Environmental Science & Technology Letters*, 9, 22-29, 10.1021/acs.estlett.1c00893,
798 2021.

799 Stockwell, W. R., Kirchner, F., Kuhn, M., and Seefeld, S.: A new mechanism for regional atmospheric
800 chemistry modeling, *J Geophys Res-Atmos*, 102, 25847-25879, 10.1029/97jd00849, 1997.

801 Stone, D., Whalley, L. K., and Heard, D. E.: Tropospheric OH and HO₂ radicals: field measurements
802 and model comparisons, *Chemical Society reviews*, 41, 6348-6404, 10.1039/c2cs35140d, 2012.

803 Sun, L., Chen, T., Jiang, Y., Zhou, Y., Sheng, L., Lin, J., Li, J., Dong, C., Wang, C., Wang, X., Zhang,
804 Q., Wang, W., and Xue, L.: Ship emission of nitrous acid (HONO) and its impacts on the marine
805 atmospheric oxidation chemistry, *Sci Total Environ*, 735, 139355, 10.1016/j.scitotenv.2020.139355,
806 2020.

807 Tan, Z., Lu, K., Ma, X., Chen, S., He, L., Huang, X., Li, X., Lin, X., Tang, M., Yu, D., Wahner, A., and
808 Zhang, Y.: Multiple Impacts of Aerosols on O(3) Production Are Largely Compensated: A Case Study
809 Shenzhen, China, *Environ Sci Technol*, 10.1021/acs.est.2c06217, 2022.

810 Tan, Z., Lu, K., Jiang, M., Su, R., Wang, H., Lou, S., Fu, Q., Zhai, C., Tan, Q., Yue, D., Chen, D., Wang,
811 Z., Xie, S., Zeng, L., and Zhang, Y.: Daytime atmospheric oxidation capacity in four Chinese

812 megacities during the photochemically polluted season: a case study based on box model simulation,
813 *Atmos Chem Phys*, 19, 3493-3513, 10.5194/acp-19-3493-2019, 2019a.

814 Tan, Z. F., Lu, K. D., Jiang, M. Q., Su, R., Dong, H. B., Zeng, L. M., Xie, S. D., Tan, Q. W., and Zhang,
815 Y. H.: Exploring ozone pollution in Chengdu, southwestern China: A case study from radical chemistry
816 to O₃-VOC-NO_x sensitivity, *Sci Total Environ*, 636, 775-786, 10.1016/j.scitotenv.2018.04.286, 2018a.

817 Tan, Z. F., Lu, K. D., Dong, H. B., Hu, M., Li, X., Liu, Y. H., Lu, S. H., Shao, M., Su, R., Wang, H. C.,
818 Wu, Y. S., Wahner, A., and Zhang, Y. H.: Explicit diagnosis of the local ozone production rate and the
819 ozone-NO_x-VOC sensitivities, *Sci. Bull.*, 63, 1067-1076, 10.1016/j.scib.2018.07.001, 2018b.

820 Tan, Z. F., Lu, K. D., Hofzumahaus, A., Fuchs, H., Bohn, B., Holland, F., Liu, Y. H., Rohrer, F., Shao,
821 M., Sun, K., Wu, Y. S., Zeng, L. M., Zhang, Y. S., Zou, Q., Kiendler-Scharr, A., Wahner, A., and Zhang,
822 Y. H.: Experimental budgets of OH, HO₂, and RO₂ radicals and implications for ozone formation in the
823 Pearl River Delta in China 2014, *Atmos Chem Phys*, 19, 7129-7150, 10.5194/acp-19-7129-2019,
824 2019b.

825 Tan, Z. F., Fuchs, H., Lu, K. D., Hofzumahaus, A., Bohn, B., Broch, S., Dong, H. B., Gomm, S.,
826 Haseler, R., He, L. Y., Holland, F., Li, X., Liu, Y., Lu, S. H., Rohrer, F., Shao, M., Wang, B. L., Wang,
827 M., Wu, Y. S., Zeng, L. M., Zhang, Y. S., Wahner, A., and Zhang, Y. H.: Radical chemistry at a rural
828 site (Wangdu) in the North China Plain: observation and model calculations of OH, HO₂ and RO₂
829 radicals, *Atmos Chem Phys*, 17, 663-690, 10.5194/acp-17-663-2017, 2017.

830 Vaughan, S., Ingham, T., K. Whalley, L., Stone, D., Evans, M. J., Read, K. A., Lee, J. D., Moller, S. J.,
831 Carpenter, L. J., Lewis, A. C., Fleming, Z. L., and Heard, D. E.: Seasonal observations of OH and HO₂
832 in the remote tropical marine boundary layer, *Atmos. Chem. Phys.*, 12, 2149–2172, 10.5194/acp-12-
833 2149-2012, 2012.

834 Wang, F., Hu, R., Xie, P., Wang, Y., Chen, H., Zhang, G., and Liu, W.: Calibration source for OH
835 radical based on synchronous photolysis, *Acta Phys Sin-Ch Ed*, 69, 2020.

836 Wang, F. Y., Hu, R. Z., Chen, H., Xie, P. H., Wang, Y. H., Li, Z. Y., Jin, H. W., Liu, J. G., and Liu, W. Q.:
837 Development of a field system for measurement of tropospheric OH radical using laser-induced
838 fluorescence technique, *Opt. Express*, 27, A419-A435, 10.1364/oe.27.00a419, 2019.

839 Wang, J., Zhang, Y., Zhang, C., Wang, Y., Zhou, J., Whalley, L. K., Slater, E. J., Dyson, J. E., Xu, W.,
840 Cheng, P., Han, B., Wang, L., Yu, X., Wang, Y., Woodward-Massey, R., Lin, W., Zhao, W., Zeng, L.,
841 Ma, Z., Heard, D. E., and Ye, C.: Validating HONO as an Intermediate Tracer of the External Cycling
842 of Reactive Nitrogen in the Background Atmosphere, *Environ Sci Technol*, 10.1021/acs.est.2c06731,
843 2023.

844 Wang, T., Wei, X. L., Ding, A. J., Poon, C. N., Lam, K. S., Li, Y. S., Chan, L. Y., and Anson, M.:
845 Increasing surface ozone concentrations in the background atmosphere of Southern China, 1994-2007,
846 *Atmos Chem Phys*, 9, 6217-6227, 10.5194/acp-9-6217-2009, 2009.

847 Wang, Y., Hu, R., Xie, P., Chen, H., Wang, F., Liu, X., Liu, J., and Liu, W.: Measurement of
848 tropospheric HO₂ radical using fluorescence assay by gas expansion with low interferences, *J Environ
849 Sci (China)*, 99, 40-50, 10.1016/j.jes.2020.06.010, 2021.

850 Whalley, L. K., Furneaux, K. L., Goddard, A., Lee, J. D., Mahajan, A., Oetjen, H., Read, K. A., Kaaden,
851 N., Carpenter, L. J., Lewis, A. C., Plane, J. M. C., Saltzman, E. S., Wiedensohler, A., and Heard, D. E.:
852 The chemistry of OH and HO₂ radicals in the boundary layer over the tropical Atlantic Ocean, *Atmos
853 Chem Phys*, 10, 1555-1576, 10.5194/acp-10-1555-2010, 2010.

854 Woodward-Massey, R., Sommariva, R., Whalley, L. K., Cryer, D. R., Ingham, T., Bloss, W. J., Ball, S.
855 M., Lee, J. D., Reed, C. P., Crilley, L. R., Kramer, L. J., Bandy, B. J., Forster, G. L., Reeves, C. E.,

856 Monks, P. S., and Heard, D. E.: Radical chemistry at a UK coastal receptor site – Part 2: experimental
857 radical budgets and ozone production, *Atmos. Chem. Phys.*, 10.5194/acp-2022-213, 2022a.

858 Woodward-Massey, R., Sommariva, R., Whalley, L. K., Cryer, D. R., Ingham, T., Bloss, W. J., Ball, S.
859 M., Lee, J. D., Reed, C. P., Crilley, L. R., Kramer, L. J., Bandy, B. J., Forster, G. L., Reeves, C. E.,
860 Monks, P. S., and Heard, D. E.: Radical chemistry at a UK coastal receptor site – Part 1: observations
861 of OH, HO₂, RO₂, and OH reactivity and comparison to MCM model predictions, *Atmos. Chem. Phys.*,
862 10.5194/acp-2022-207, 2022b.

863 Xia, M., Wang, T., Wang, Z., Chen, Y., Peng, X., Huo, Y., Wang, W., Yuan, Q., Jiang, Y., Guo, H., Lau,
864 C., Leung, K., Yu, A., and Lee, S.: Pollution-Derived Br₂ Boosts Oxidation Power of the Coastal
865 Atmosphere, *Environ Sci Technol*, 10.1021/acs.est.2c02434, 2022.

866 Xia, S.-Y., Zhu, B., Wang, S.-X., Huang, X.-F., and He, L.-Y.: Spatial distribution and source
867 apportionment of peroxyacetyl nitrate (PAN) in a coastal region in southern China, *Atmos Environ*, 260,
868 10.1016/j.atmosenv.2021.118553, 2021.

869 Xu, W., Ovadnevaite, J., Fossum, K. N., Lin, C., Huang, R.-J., Ceburnis, D., and O’Dowd, C.: Sea
870 spray as an obscured source for marine cloud nuclei, *Nature Geoscience*, 15, 282-286, 10.1038/s41561-
871 022-00917-2, 2022.

872 Yang, X., Lu, K., Ma, X., Gao, Y., Tan, Z., Wang, H., Chen, X., Li, X., Huang, X., He, L., Tang, M.,
873 Zhu, B., Chen, S., Dong, H., Zeng, L., and Zhang, Y.: Radical chemistry in the Pearl River Delta:
874 observations and modeling of OH and HO₂ radicals in Shenzhen in 2018, *Atmos Chem Phys*, 22,
875 12525-12542, 10.5194/acp-22-12525-2022, 2022a.

876 Yang, X., Lu, K., Ma, X., Gao, Y., Tan, Z., Wang, H., Chen, X., Li, X., Huang, X., He, L., Tang, M.,
877 Zhu, B., Chen, S., Dong, H., Zeng, L., and Zhang, Y.: Radical chemistry in the Pearl River Delta:
878 observations and 2 modeling of OH and HO₂ radicals in Shenzhen 2018, 10.5194/acp-2022-113, 2022b.

879 Yang, X., Lu, K., Ma, X., Liu, Y., Wang, H., Hu, R., Li, X., Lou, S., Chen, S., Dong, H., Wang, F.,
880 Wang, Y., Zhang, G., Li, S., Yang, S., Yang, Y., Kuang, C., Tan, Z., Chen, X., Qiu, P., Zeng, L., Xie, P.,
881 and Zhang, Y.: Observations and modeling of OH and HO₂ radicals in Chengdu, China in summer 2019,
882 *The Science of the total environment*, 772, 144829-144829, 10.1016/j.scitotenv.2020.144829, 2021a.

883 Yang, Y., Li, X., Zu, K., Lian, C., Chen, S., Dong, H., Feng, M., Liu, H., Liu, J., Lu, K., Lu, S., Ma, X.,
884 Song, D., Wang, W., Yang, S., Yang, X., Yu, X., Zhu, Y., Zeng, L., Tan, Q., and Zhang, Y.: Elucidating
885 the effect of HONO on O₃ pollution by a case study in southwest China, *Sci Total Environ*, 756,
886 144127, 10.1016/j.scitotenv.2020.144127, 2021b.

887 Zeren, Y., Zhou, B., Zheng, Y., Jiang, F., Lyu, X., Xue, L., Wang, H., Liu, X., and Guo, H.: Does Ozone
888 Pollution Share the Same Formation Mechanisms in the Bay Areas of China?, *Environ Sci Technol*,
889 10.1021/acs.est.2c05126, 2022.

890 Zhang, G., Hu, R., Xie, P., Lou, S., Wang, F., Wang, Y., Qin, M., Li, X., Liu, X., Wang, Y., and Liu, W.:
891 Observation and simulation of HO_x radicals in an urban area in Shanghai, China, *Sci Total Environ*,
892 810, 152275, 10.1016/j.scitotenv.2021.152275, 2022a.

893 Zhang, G., Hu, R., Xie, P., Lu, K., Lou, S., Liu, X., Li, X., Wang, F., Wang, Y., Yang, X., Cai, H., Wang,
894 Y., and Liu, W.: Intercomparison of OH radical measurement in a complex atmosphere in Chengdu,
895 China, *Sci Total Environ*, 155924, 10.1016/j.scitotenv.2022.155924, 2022b.

896 Zhu, B., Huang, X.-F., Xia, S.-Y., Lin, L.-L., Cheng, Y., and He, L.-Y.: Biomass-burning emissions
897 could significantly enhance the atmospheric oxidizing capacity in continental air pollution, *Environ.*
898 *Pollut.*, 285, 10.1016/j.envpol.2021.117523, 2021.

899 Zhu, Y., Wang, Y., Zhou, X., Elshorbany, Y. F., Ye, C., Hayden, M., and Peters, A. J.: An investigation

900 into the chemistry of HONO in the marine boundary layer at Tudor Hill Marine Atmospheric
901 Observatory in Bermuda, *Atmos Chem Phys*, 22, 6327-6346, 10.5194/acp-22-6327-2022, 2022.
902 Zou, Z., Chen, Q., Xia, M., Yuan, Q., Chen, Y., Wang, Y., Xiong, E., Wang, Z., and Wang, T.: OH
903 measurements in the coastal atmosphere of South China: missing OH sinks in aged air masses,
904 *EGUsphere*, 2022, 1-47, 10.5194/egusphere-2022-854, 2022.
905